Journal of Biomedical Optics

SPIEDigitalLibrary.org/jbo

Wide-field spectral imaging of human ovary autofluorescence and oncologic diagnosis via previously collected probe data

Timothy E. Renkoski
Kenneth D. Hatch
Urs Utzinger

SPIE

Wide-field spectral imaging of human ovary autofluorescence and oncologic diagnosis via previously collected probe data

Timothy E. Renkoski,[a] Kenneth D. Hatch,[b] and Urs Utzinger[a,b,c]
[a]University of Arizona, College of Optical Sciences, 1630 East University Boulevard, Tucson, Arizona 85721
[b]University of Arizona, Arizona Health Sciences Center, Department of Obstetrics and Gynecology, North Campbell Avenue, Tucson, Arizona 85724
[c]University of Arizona, Department of Biomedical Engineering, 1127 East James E. Rogers Way, Tucson, Arizona 85721

Abstract. With no sufficient screening test for ovarian cancer, a method to evaluate the ovarian disease state quickly and nondestructively is needed. The authors have applied a wide-field spectral imager to freshly resected ovaries of 30 human patients in a study believed to be the first of its magnitude. Endogenous fluorescence was excited with 365-nm light and imaged in eight emission bands collectively covering the 400- to 640-nm range. Linear discriminant analysis was used to classify all image pixels and generate diagnostic maps of the ovaries. Training the classifier with previously collected single-point autofluorescence measurements of a spectroscopic probe enabled this novel classification. The process by which probe-collected spectra were transformed for comparison with imager spectra is described. Sensitivity of 100% and specificity of 51% were obtained in classifying normal and cancerous ovaries using autofluorescence data alone. Specificity increased to 69% when autofluorescence data were divided by green reflectance data to correct for spatial variation in tissue absorption properties. Benign neoplasm ovaries were also found to classify as nonmalignant using the same algorithm. Although applied *ex vivo*, the method described here appears useful for quick assessment of cancer presence in the human ovary. [DOI: 10.1117/1.JBO.17.3.036003]

Keywords: fluorescence; fluorescence spectroscopy; image analysis; medical imaging; multispectral imaging; ultraviolet.

Paper 11452 received Aug. 21, 2011; revised manuscript received Dec. 2, 2011; accepted for publication Jan. 4, 2012; published online Mar. 29, 2012.

1 Introduction

Ovarian cancer is a particularly deadly disease that, as of 2010, had a five-year survival rate of 46% in the United States.[1] Currently, no screening test is capable of consistently detecting the disease at the early, localized stage.[1] For this reason, only 15% of all ovarian cancer cases are diagnosed at the localized stage in which the disease is highly curable.[1] It is well documented that approximately 90% of ovarian cancers arise in the epithelium,[2] or surface layer of the ovary, which validates the feasibility of laparoscopy for early ovarian cancer screening.

One promising approach for disease detection and localization in numerous organ sites has been spectroscopic evaluation of endogenous tissue contrast using both fluorescence and reflectance-based techniques.[3] Autofluorescence spectroscopy has been applied to distinguish malignancy in tissues of the human lung, breast, skin, oral cavity, cervix, gastrointestinal tract, brain, bladder, and ovary.[4] These studies of native tissue fluorescence, including both steady-state and time-resolved measurements, have been extensively reviewed.[3,5–8] Diffuse reflectance spectroscopy (DRS) has likewise been applied to all the tissues mentioned above, with emphasis on the skin,[9,10] breast,[11–15] brain,[16–18] and cervix.[19–21]

While "point" spectroscopy techniques based on autofluorescence, diffuse reflectance, or some combination of the two have shown promise for noninvasive optical biopsy, these methods have not gained common clinical usage, let alone supplanted the standard needle biopsy or excisional biopsy. The spectroscopic diagnostic devices that have reached commercialization[22–24] have combined both spectral and spatial information through spectral imaging—also called "multispectral" or "hyperspectral" imaging. This method is realized either through the collection of images at various wavelength bands or by the acquisition of spectra at a multitude of point locations. Recently, Balas[25] reviewed the status of spectral bioimaging. Spectral imaging of autofluorescence seems to have found its niche as a means of improving the visualization of neoplastic lesions on the cervix,[23] in the mouth,[26] and, endoscopically, in the lungs[22] and the gastrointestinal tract.[24]

Another promising optical biopsy method for cancer is the time-resolved version of autofluorescence imaging, known as fluorescence lifetime imaging (FLIM). In this method images are constructed from spatially resolved fluorescence lifetime measurements. Fluorescence lifetimes, like autofluorescence intensity and spectral shape, have been proven useful in determining tissue pathological state. FLIM endoscopes and microscopes have been developed for distinguishing cancer in the lungs,[27] skin,[28] oral cavity,[29] and brain.[30] FLIM provides benefits over steady-state fluorescence imaging that include insensitivity to illumination intensity and reduced sensitivity to tissue optical properties. While FLIM is a promising imaging modality, it also has drawbacks including increased instrumentation complexity and measurement acquisition time. FLIM will not be discussed in detail here as the spectral imager of this study incorporated only steady-state fluorescence acquisition.

Address all correspondence to: Urs Utzinger, University of Arizona, Department of Biomedical Engineering, 1127 East James E. Rogers Way, Tucson, Arizona 85721; Tel: 520-621-5420; E-mail: utzinger@email.arizona.edu.

0091-3286/2012/$25.00 © 2012 SPIE

Speaking again of spectral imaging in general, clinicians typically use spectral images together with their own experience to select tissue locations to biopsy and analyze with standard histology, the gold standard for diagnosis. However, automated analysis of tissue spectral images renders optical diagnosis more objective and reduces the need for an experienced clinician with optical knowledge to perform the evaluation. For example, tissue images can be transparently overlaid with false-color maps indicating a simplified optical diagnosis. Several groups have demonstrated spectral image analysis enhancements with varying degrees of automation.[31–37]

In the study described here, we have applied a 365 nm-excitation multispectral imager (MSI) to freshly resected whole human ovaries, collecting autofluorescence images in eight different spectral bands spanning the 400 to 640 nm visible range as well as reflectance images in four different visible spectral bands. To our knowledge, this is the first wide-field spectral imaging study of human ovary autofluorescence of this magnitude. We diagnostically map large areas of tissue by utilizing linear discriminant analysis and a library of previously-collected fluorescence probe spectra (from ovarian biopsies of histology-confirmed diagnosis). The incorporation of training data from a second instrument was necessary due to the impracticality of extensive biopsy of all the ovaries imaged in the study. We elaborate a process for transforming the probe spectra, enabling one-to-one comparison with MSI spectra. Sensitivity of 100% and specificity of 51% were obtained using fluorescence data alone for the diagnostics. Specificity was increased to 69% after correcting autofluorescence data for variation in tissue optical properties. The correction used was a division of measured autofluorescence by green reflectance data also collected by the MSI.

2 Materials and Methods

2.1 *Clinical Studies and Ovarian Pathology*

Multispectral fluorescence images of 49 whole human ovaries from 30 patients were collected *ex vivo* through a clinical study at the University Medical Center of the Arizona Health Sciences Center at the University of Arizona in Tucson. The study (A02.31/OB/GYN) was approved by the Institutional Review Board (IRB) of the University of Arizona, and informed consent was obtained from each patient before tissue imaging occurred. All study participants were women undergoing planned oophorectomy either for disease treatment or as prophylaxis. The average patient age was 58, and 25 of the 30 patients were postmenopausal.

In this study an MSI with 365-nm illumination was used to perform fluorescence spectroscopy. The goal was to define regions of abnormal tissue as well as any tumor margins that might be present in images by observing spatial variations in autofluorescence. A central assumption was that tissue pathology could vary across a single wide-field image. It was, therefore, desirable to have histopathological results from many small tissue areas in order to validate diagnostic mapping; however, time restrictions of the pathologist prevented each ovary from being completely sectioned and microscopically analyzed. Instead, the standard gross pathology assessment was performed; that is, one to three sections of each ovary were made and analyzed to determine a diagnosis.

In the absence of complete sectioning and histopathology of the whole ovaries in the imaging study, we elected to utilize a second dataset collected previously as part of a nonimaging (single-point) ovarian autofluorescence study (#02-113/OB/GYN).In that study, small excisional biopsies were collected from each ovary at the site of each probe-based spectral measurement and sectioned for microscopic analysis. This single-point spectral dataset and corresponding histopathology were used to train a classifier that we applied to the tissue spectral images collected by the MSI.

For our purposes, it was useful to group all of the numerous ovarian pathologies into four general categories: normal (no structures except stroma, epithelium, corpus albicans, and corpus luteum), benign neoplasm (abnormal growth without invasive areas), cancer (invasion of carcinoma into the ovary), and endometriosis (growth of both endometrial glands and stroma on the ovary). Included in our analysis are 92 sets of multispectral images collected from 24 ovaries of normal pathology, 10 sets of multispectral images collected from three ovaries of benign neoplasm pathology, 12 sets of multispectral images collected from two ovaries of cancer pathology, and 30 sets of multispectral images collected from six ovaries of endometriosis pathology. Excluded measurements are detailed in Sec. 3.7. The diagnostic classifier was trained using only ovaries of normal and cancer pathological diagnoses but then applied to ovaries of all four aforementioned pathologies. Histopathology was used as the diagnostic gold standard.

2.2 *MSI*

A multispectral imaging system (SEAtreat, Apogen Technologies, Inc., now QinetiQ North America, San Diego, CA), henceforth referred to as the MSI, was used for automated acquisition of both fluorescence and reflectance images of whole ovaries. The imager, whose simplified optical layout is presented in Fig. 1, has a fixed focus at a working distance of 30 cm, field-of-view 40 mm × 33 mm, and resolution 580 × 475 pixels. The device acquires four spatially registered images simultaneously on a single charge-coupled device (CCD) using a patented technique,[38,39] Quad-Prism Aperture

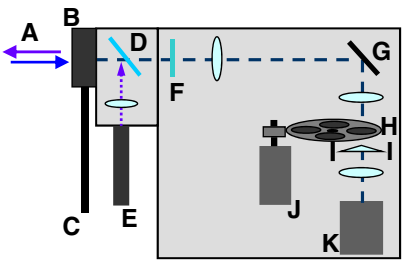

Fig. 1 Simplified optical layout of the multispectral imaging device (SEAtreat, Apogen Technologies, Inc., now QinetiQ North America, San Diego, CA). Each lens depicted represents multiple elements. The system used single excitation of 365 nm and eight fluorescence emission bands covering the visible range (400 to 640 nm). The system used white light illumination when capturing crossed-polarization reflectance images. QPAS allowed simultaneous capture of four uniquely filtered images on a single CCD.

Splitting (QPAS). Fluorescence illumination is provided by the MSI using a short-arc mercury lamp (LC6 series, Hamamatsu, Bridgewater, NJ) filtered to include only the ultraviolet line emission at 365 nm and coupled to a fiber-optic bundle that carries the light from the lamp to the imaging head. Ultraviolet (UV) light is projected onto the tissue at a power density of 18 mW/cm^2 and excites a broad spectrum of autofluorescence, which is collected, divided into four parallel optical paths (each uniquely bandpass-filtered), and imaged onto four quadrants of a single CCD. A motorized filter wheel allows rapid exchange of the bandpass quad-filter, and thus a total of eight images are collected by two consecutive exposures of the CCD. The eight fluorescence emission bandpass filters effectively cover the spectrum from 400 to 640 nm with little overlap. The filter center wavelengths are 420, 440, 455, 485, 510, 530, 560, and 600 nm.

For reflectance imaging, a halogen bulb provides linearly polarized white light illumination at a power density of 8 mW/cm^2. A different set of quad-filters is rotated into the optical path for collection of each set of reflectance images. Each reflectance quad-filter has blue, green, red, and near-infrared quadrants and is masked by a polarizer whose transmission axis is either crossed or parallel in comparison to the polarization of the illumination. Light that is reflected specularly at the tissue surface is highly attenuated by the crossed polarizer.

2.3 *Multispectral Imaging Procedure*

Oophorectomy was typically laparoscopic, but in some cases an open surgery was performed. Whole ovaries and attached fallopian tubes were severed via electrosurgery. Removal of tissue from the body occurred sometimes through one of the laparoscopic incisions (after placement of ovary in a protective plastic bag) and sometimes vaginally (in coordination with a hysterectomy. Each ovary was bathed in room temperature saline solution and transported in a metal bowl. Care was taken to always grasp the ovaries by the fallopian tube to avoid damage to the fragile ovarian epithelium. Ovaries were taken to a darkened room and placed on a plastic Petri dish for imaging. A solution of phosphate-buffered saline (PBS), glucose, and L-glutamine was used to rinse blood from the ovarian surface and to maintain moisture during imaging. Imaging typically began within 30 min after loss of blood supply to organ and required 5 to 8 min from start to finish. In all cases, imaging began less than 60 min after loss of blood supply to organ. Data collection within 90 min of biopsy has been shown to minimize difference of *ex vivo* fluorescence measurements compared to *in vivo*.[40] Typical integration times were 100 ms for fluorescence images, 5 ms for parallel-polarization reflectance images, and 13 ms for crossed-polarization reflectance images.

2.4 *Single-Point Spectral Data*

Single-point autofluorescence data were collected from fresh 5- to 10-mm-sized ovarian tissue biopsies as part of a previous study also at the University Medical Center at the Arizona Health Sciences Center (#02-113/OB/GYN).In total, 249 single-point spectra were collected from 49 patients, with 186 of the spectra being collected from ovarian tissue deemed histopathologically normal, 25 being collected from tissue deemed cancer, 10 collected from tissue deemed endometriosis, and eight from tissue deemed benign neoplasm. The remaining 20 measurements could not be used because pathology was unavailable.

The device used to collect single-point spectral data was previously described;[41,42] briefly, a spectrofluorometer (FluoroLog 3-22, JY Horiba, Edison, NJ) using double excitation and emission spectrographs coupled to a custom fiber-optic probe that was used to interrogate a tissue spot of 800-micron diameter. The six-around-one fiber configuration probe was positioned in contact with the surface epithelium allowing the weight of the probe to contact the tissue. Spectra were recorded from three to four locations on each biopsy. Biopsies were placed in chilled Roswell Park Memorial Institute (RPMI) culture medium (Media Tech, Herndon, VA) and transported to the optics laboratory. Typically, fluorescence measurements were performed within 60 min after removal. Subsequently, tissue was fixed and processed with standard histological procedures. A pathologist examined each ovarian biopsy at University Medical Center, and pathology results were obtained.

The collected single-point data was in the form of an excitation emission matrix (EEM) with 14 different excitation wavelengths from 270 to 550 nm. Data were calibrated for variations in excitation power as well as spectral sensitivity of the detector.

2.5 *Single-Point Spectral Data Conversion Process*

The single-point autofluorescence data EEM are of relatively high spectral resolution, sampled every 5 nm, while the MSI data are low-resolution "spectra," which include only eight measurements over the same emission range (see Fig. 2).The eight-point MSI spectra are not spectra in the strictest sense because each spectral image is weighted by the system's spectral sensitivity, which varies with the transmission characteristics of the optical filters used for collection. For one-to-one comparison of

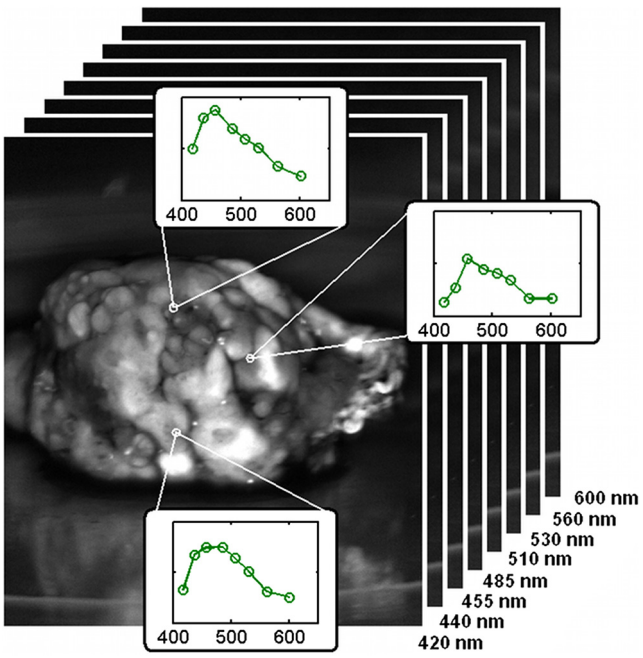

Fig. 2 Background: Multispectral image stack. Eight autofluorescence images of a whole human ovary were excited by 365-nm-filtered mercury lamp and each captured using a different bandpass filter between 400 and 640 nm. Foreground: An eight-point fluorescence spectrum of the tissue can be extracted at each pixel, given spatial registration of all the stack images.

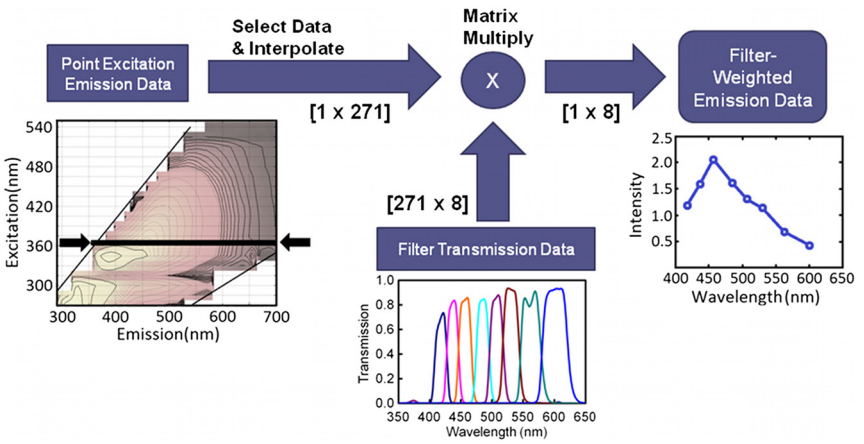

Fig. 3 Conversion of single-point spectral data. The input data was an excitation emission matrix (EEM) such as the one plotted at left. The emission spectrum for 365-nm excitation was selected from the EEM for processing, while the remaining data was discarded. At each collection wavelength, the fluorescence intensity of the measured spectrum was multiplied by the transmission of a filter used for multispectral imaging. These products were then summed over all wavelengths at which filter data existed. A matrix multiplication carried out this process for each of eight emission filters. (Matrix dimensions are given in brackets.) The result, plotted versus filter center wavelength, was an eight-point autofluorescence spectrum weighted for direct comparison to data from the MSI.

these two datasets, we needed either to weight the single-point EEM data with the spectral sensitivity characteristics of the MSI yielding eight-point filter-weighted spectra or to convert the eight-point MSI spectra into true spectra.

Mathematically, it was easier to transform the single-point EEM spectra to the eight-point spectral space of the MSI. We accomplished this by multiplying the single-point spectra by the measured sensitivity characteristics of the MSI at each filter configuration. This filter-weighting process is illustrated in Fig. 3. Notice that each horizontal line of data in the single-point EEM corresponds to a different excitation wavelength. We utilized only the portion of the EEM corresponding to 365-nm fluorescence excitation (denoted with black line and arrows in Fig. 3), as this was the only excitation wavelength of the MSI.

2.6 *MSI Data Pre-Processing and Calibration*

Image processing and analysis was performed using MATLAB (The MathWorks, Natick, Massachusetts). Each set of raw image data from the CCD was 1024×1280 pixels and contained four images—one 512×640 pixel image from each quadrant. A corresponding set of dark images was captured for each image set. Manufacturer-provided code was used to perform image pre-processing as follows. The first step involved breaking the composite image into four separate images. Then spatial registration of the images and correction of distortion were performed. Next, dark subtraction and flat field illumination correction were applied. Scale factors were used to account for differences in integration time.

We implemented additional pre-processing steps to the original MATLAB code. Background subtraction of a nonfluorescing standard was applied to correct for device autofluorescence. The subtracted background measurement was taken in a dark room with imager viewing a distant, nonfluorescent black cloth. The power level of the UV source was measured daily with a power meter, and any variation was corrected for in the images via a scale factor.

The MSI data and single-point spectra compared in this study were collected by two different devices utilizing different means of wavelength selection and different detectors. As a result, calibration for the spectral response of each system was required. To eliminate device-dependent differences in collected spectra, solid and liquid fluorescence standards were imaged with the MSI and also measured with the spectrofluorometer. The solid standards used were tetraphenylbutadiene (TPB) and rhodamine B (Starna Ltd., Hainault, UK), while the liquid standard was fluorescein in a quartz cuvette (Molecular Probes, Eugene, OR).

For a one-to-one comparison of the measured eight-point fluorescence spectra to the known spectra provided by the manufacturer of the fluorescence standard, it was necessary to weight the known fluorescence spectrum of each standard with the spectral sensitivity characteristics of the MSI (through the process illustrated previously in Fig. 3).

Division of the calculated eight-point fluorescence emission spectrum of a fluorescence standard by its measured eight-point spectrum yielded a set of correction factors for the absolute spectral response of the MSI. Applying these multiplicative correction factors to the spectral images captured by the device allowed calibrated fluorescence emission spectra to be extracted from the collection of uniquely filtered, spatially registered images.

2.7 *Intensity Matching of MSI Data to Single-Point Data*

Finally, to compare the single-point emission spectra and the MSI spectra, only intensity equalization was lacking. We aimed to calculate a single scale factor that would adjust the fluorescence intensities collected by the spectrofluorometer to be on the same level as those collected by the MSI. Instead of comparing measurement intensities of fluorescence standards between the two systems, we found that calibrating the intensity distributions of all measurements made on ovaries deemed normal by histopathological evaluation was an appropriate procedure.

The single-point measurement intensity histogram (composed of 186 measurements on normal tissue) and MSI data intensity histogram (composed of 92 measurements on normal

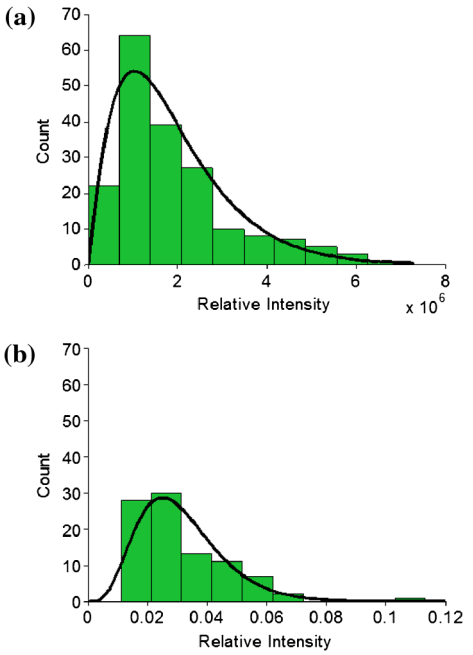

Fig. 4 Histograms of autofluorescence intensities at 455-nm filter center wavelength, only including tissues confirmed normal by histopathology. (a) Filter-weighted, previously collected single-point measurements of ovarian biopsies. (b) Multispectral imaging measurements (on whole ovaries) averaged over the pixels in the ROI of a single ovary. Each histogram was fit to a gamma distribution. Datasets from spectrofluorometer and MSI were intensity equalized based on statistics of these measurements.

tissue), both shown in Fig. 4, were produced as follows. Single-point measurements were first converted to eight-point spectra as described previously. Only 455-nm measurement intensities were included in the histogram because they typically represented the maximum of the spectrum. For the MSI data, a unique region of interest (ROI) was first manually selected in all images. (In order to lessen the effect of camera view angle on image intensity, the ROIs were selected to include only tissue approximately normal to the camera). Then, for each image, the 455-nm-filtered image intensity was averaged over the ROI pixels. These average pixel intensities were used in constructing the intensity histogram of MSI data.

Two methods of intensity equalizing the datasets were tested. In the first method, a ratio of the means of the two intensity distributions was used as a scale factor. For the second method, a gamma distribution was fitted to each intensity histogram, and the scale factor used was a ratio of the peak intensity of each fitted gamma distribution.

2.8 *Classification Method and Optimum Preparation of Data*

Linear discriminant analysis (LDA) is a statistical method useful for predicting whether a measurement belongs to one class or another, and to perform LDA, a set of training measurements of known class is required. In our case the chosen measurement classes were normal and cancer, and our library of single-point spectra and associated gold-standard pathologies served as the training data. In LDA, each measurement can be considered to lie somewhere in an N-dimensional "measurement space." Training measurements define the distribution of each class within the N-dimensional space. Given a measurement, LDA calculates which class (and distribution) the measurement most likely belongs to. In this study, LDA was performed by using the "classify" function included in the MATLAB statistics toolbox.

Before classification via LDA, it was desirable to reduce data dimensionality, N. Smaller N reduces computational load and, up to a point, increases the effectiveness of LDA. We applied principal component analysis (PCA) to the data sets by calculating the covariance matrix of the data and decomposing it into eigenvectors and eigenvalues. The highest scoring eigenvectors, or principal components (PCs), represent a basis for a lower dimensional space that measurements can be mapped to. PCA maximizes the variance of the data that can be represented by a given number of PCs.

The appropriate number of PCs to use for LDA was determined by performing jackknife analysis on the set of training measurements and varying the number of PCs used for the measurement space. One measurement at a time was removed from the dataset and PCA applied to the remaining measurements. LDA was then used to classify the removed measurement, and the process was repeated for each measurement, always replacing one measurement and removing another. Sensitivity and specificity of the classification were calculated and used to select an appropriate number of PCs and thus the final data dimensionality. Jackknife analysis was similarly used to determine whether classification would be more effective using unnormalized or normalized data.

2.9 *Diagnostic Tissue Mapping*

Many choices exist for effectively displaying multispectral image information. Each single specific wavelength image can be observed in gray scale, or three specific wavelength images may be observed together in a false-color red, green, and blue (RGB) image. However, eight specific wavelength images cannot be displayed in full spectral detail in a single image of three-color channels.

The approach we took was to statistically analyze the spectral data at each image pixel and then visually display the results in a binary image. LDA was applied to classify the measured spectrum from each pixel in an image ROI. The LDA training set consisted of a library of 211 single-point spectra. Prior to classification, PCs calculated from the training set were used to map the test spectra to a new measurement space. For every multispectral image set, a diagnostic tissue map was produced by overlaying the ROI of a specific wavelength fluorescence image with color-coded pixels. Pixels that classified as normal were colored green, and pixels that classified as cancer were colored red, as will be seen in later figures.

3 Results

3.1 *Multispectral Imager Calibration*

Correction factors for the absolute spectral response of the MSI were calculated as described in Sec. 2.6. Results from measurements on three relevant fluorescence standards are compared in Fig. 5. The plotted data illustrates that longer wavelength bands must be scaled up in intensity relative to images at shorter bands. The system sensitivity therefore appears to be lowest at the longest wavelengths imaged. Comparison of the three normalized curves in Fig. 5 shows excellent agreement between the fluorescence measurements of TPB and fluorescein except at

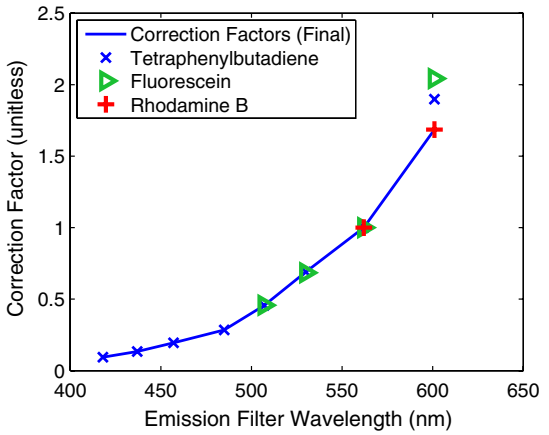

Fig. 5 Normalized correction factor for the absolute spectral response of the multispectral imager (MSI), calculated using three different fluorescence standards. Images captured using filters of longer center wavelength must be scaled up in intensity to compensate for lower system sensitivity at longer wavelengths. Tetraphenylbutadiene correction factors were selected for scaling the first seven imaging bands. The correction factor for the 600-nm filter band was chosen according to the results from the Rhodamine B standard.

the longest wavelength emission filter. However, both TPB and fluorescein fluoresce weakly at 600 nm, while rhodamine B fluoresces significantly there. For this reason, the first seven correction factors are selected from TPB results, but the final correction factor is chosen to match the rhodamine B results.

3.2 *Inter-Device Spectral Shape Correction*

Using gross histopathology to group fluorescence spectra, we compare the average MSI-collected spectra of normal, cancer, and benign tissues, where the benign group includes both benign neoplasm and endometriosis. Each average spectrum is calculated by taking the mean of each spectrum from all ROI pixels of each image and then averaging over all the tissue images of the same histopathology. Results are shown in Fig. 6(a) with the average spectra from the single-point device shown in Fig. 6(b) for reference. In both the imaging study and the single-point study, the average fluorescence intensity from normal ovarian tissue is much higher than from cancer tissue. In the imaging study, the average benign fluorescence was highest of the three measurement groups. Although inconsistent with the single-point study result, this finding agrees with that of Brewer et al.,[41] and we note that the benign group of measurements was small in the single-point study.

The average normal spectrum acquired with the MSI [Fig. 6(a)] displays a different shape compared to the single-point device spectrum [Fig. 6(b)]. The fluorescence peak is red shifted, and the relative intensities at the longest wavelengths are enhanced. Although single-point measurements were collected from a separate set of normal ovaries, we expect the average fluorescence properties of the tissues to be very similar. Gebhart et al.[43] published a comparative study of single-point and spectral imaging fluorescence measurements from tissue phantoms and observed redshifted spectra; the effect they observed was, however, less pronounced. Dividing the average spectra of the two devices yields monotonic functions, shown in Fig. 6(c), which are similar for spectra of both normal and cancer tissues. The dissimilar device spectra could therefore stem from differences in the illumination-collection geometries

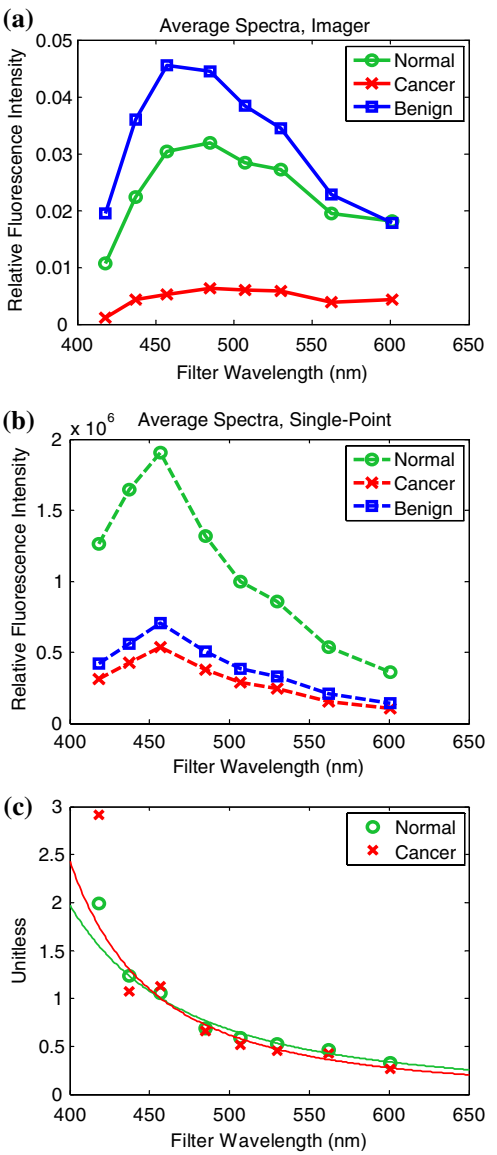

Fig. 6 (a) Average calibrated fluorescence spectra from normal, cancer, and benign ovaries measured with the multispectral imager (MSI). (b) Average calibrated fluorescence spectra from normal, cancer, and benign ovarian biopsies measured as part of a previous study using single-point spectroscopy. All measurements were captured *ex vivo* with 365-nm excitation. (c) Results of dividing the average spectra collected by each device when observing normal tissue and when observing a cancer tissue. These data have each been normalized and fitted with a second-order curve. The curve from normal tissue is used to correct the shape of spectra captured by the MSI.

of the two systems. To equalize the two datasets prior to classification, all the MSI spectra were shape-adjusted by multiplication with the normal curve shown in Fig. 6(c). Henceforth, we refer to them as shape-corrected spectra.

3.3 *Correction for Spatial Variation of Tissue Optical Properties*

We observed that the presence of blood or increased vascularity on or near the ovarian surface seemed to reduce measured autofluorescence and to interfere with classification. Tissue optical properties (absorption and scattering) affect both the

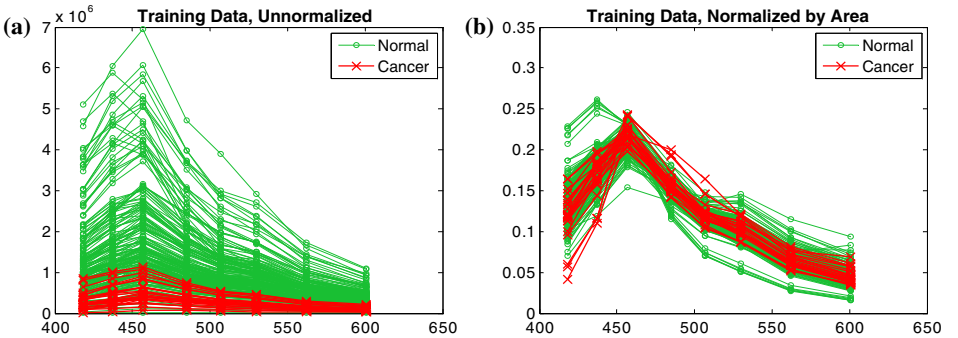

Fig. 7 (a) Filter-weighted unnormalized training data measurements show a trend of lower autofluorescence intensity in histopathology-confirmed cancerous biopsies. (b) Filter-weighted training data measurements normalized by area under curve show no obvious spectral feature distinguishing normal and cancerous biopsies.

propagation of excitation light into the tissue and the ability of emitted autofluorescence to escape the tissue for collection by the imaging system. To correct for the absorption effects of blood and hypervascularity, we divided the fluorescence images by a green-channel crossed-polarization reflectance image. Correction using blue and red reflectance images was attempted as well but produced less favorable results. The simple correction method we use has similarity to the one employed by Zeng,[44] who divided skin fluorescence spectra by reflectance measurements at corresponding wavelengths as a first-order correction for tissue absorption and scattering effects. Our correction is also similar to the one used by Qu,[45] who divided tissue fluorescence images by crossed polarization reflectance images captured at the excitation wavelength to correct for tissue absorption and geometrical effects. To avoid disturbing the average intensity level of the fluorescence images, we normalized each reflectance image to have an average value of one over the ROI prior to the division.

3.4 *Optimum Preparation of Data for Classification*

Jackknife analysis was performed on the training set spectra (single-point probe spectra) to determine whether classification of normalized spectra or unnormalized spectra would be more effective. The sensitivity realized using unnormalized data (100%) was much higher than when using data normalized by area (56%). Specificity realized using unnormalized data (71.5%) was comparable to that using data normalized by area (73.1%). Figure 7 illustrates the advantage of using unnormalized data. The unnormalized data display an obvious trend of lower-intensity cancer autofluorescence measurements and higher-intensity normal autofluorescence measurements. Normalizing the training data spectra by area emphasizes spectral shape; however, critical intensity information from measurement to measurement is lost in the process.

Figure 8 shows the two highest-scoring eigenvectors from PCA of the single-point training spectra. The first eigenvector, or principal component (PC), resembles the average eight-point spectrum of the training set. The second eigenvector allows lower (violet) or higher (blue, green, red) wavelength bands to be weighted more heavily. These two eigenvectors combined to represent 99.6% of the variance of the training data, which suggests that two PCs sufficiently represent the data.

To confirm the appropriate number of PCs for representation of the measurements, additional jackknife analysis was performed on the training set, and the results are displayed in Table 1. The combined sensitivity and specificity of classification was maximized when three PCs were used; however, two PCs were chosen for measurement representation because the lower number of PCs increases the model robustness.

3.5 *Tissue Classification (Mapping) Via LDA*

Autofluorescence images from the MSI were preprocessed, calibrated, and intensity equalized to the training set measurements as described previously. The eight-point spectra were then shape-corrected to match the training set spectra. Component loadings of both the test set and training set spectra were calculated based on PCA of the training set spectra (Fig. 8). Figure 9 shows the two classes of training set measurements plotted in the space of training set PC 1 and PC 2. The diagonal line designates the boundary for classifying a test measurement into the normal or cancer class. Sequentially, LDA was used to classify each ROI pixel of each tissue image into one of these two training set classes.

Figure 10 displays classification results from a single normal ovary with a bumpy surface. The RGB reflectance image

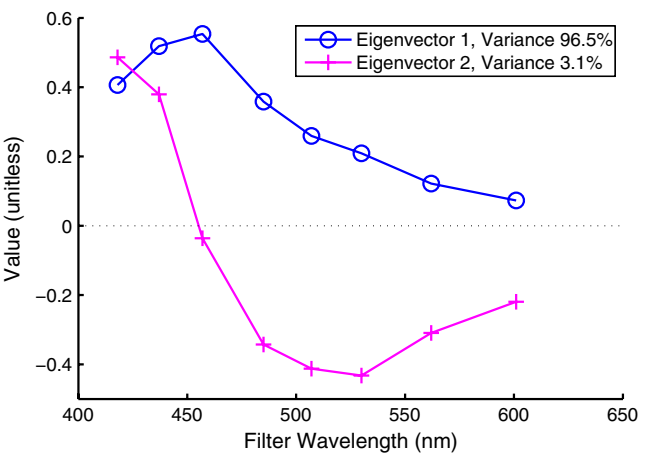

Fig. 8 Results of principal component analysis (PCA). The first eigenvector, or principal component (PC), represents the vast majority of the variance in the training dataset, and its shape closely resembles the average spectrum. These facts indicate that the dataset can be classified fairly well by considering only the intensity of a measurement. The second PC accounts for a small fraction of the dataset variance and can be used to emphasize portions of the spectrum lower or higher than 455 nm.

Table 1 Results of jackknife analysis on the training data using different numbers of PCs.

Principal comp.'s	Sensitivity (%)	Specificity (%)	Sensitivity +specificity
1	100	65.6	165.6
2	100	71.5	171.5
3	100	74.7	174.7
4	100	71.5	171.5
5	92	74.7	166.7

PCs = principal components.

[Fig. 10(a)] shows abundant vasculature near the top and left of the image ROI, especially in the creases of the uneven tissue. Plots on the right side of the figure show distributions of the MSI data PC loadings (including only pixel data from inside the ROI) laid over distributions of the normal training set data PC loadings. Figure 10(b) shows PC loadings representing MSI spectra that are uncorrected for spectral shape as discussed in Sec. 3.2. These data do not overlap well with the training set. This is consistent with the previous observation that the training and test sets produced differently shaped average spectra. The color-coded classification map [Fig. 10(c)] shows that after spectral shape correction, 76% of pixels classify like normal tissue
(pixels shown in green) and 24% like cancer tissue (pixels shown in red). Shape correction greatly improved overlap of the image data with the training data [Fig. 10(d)], and we observed a similar effect for spectra from other samples. When applying the correction for spatial variation in tissue optical properties, improved classification results were achieved [Fig. 10(e)]. Figure 10(f) shows that division of the shape-corrected fluorescence data by green reflectance data has shifted many of the ROI pixels from the cancer classification region at left of the decision boundary to the normal region at right. The total area covered by the cloud of data points is also reduced.

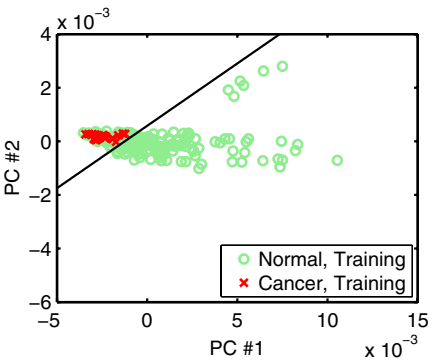

Fig. 9 Training set measurements, plotted in the space of the first two principal components (PCs). Normal and cancer groups overlap. Diagonal line is the decision boundary used for classification of test group measurements. Generally, PC #1 accounts for variations in intensity of measured spectra, and PC #2 accounts for differences in shape of measured spectra.

Presented in Fig. 11 are the classification results from imaging of a single cancer ovary. As seen in the reflectance image [Fig. 11(a)], this ovary had grown to an unusual size exceeding the camera field of view. Distributions of the image data PC loadings [Fig. 11(b), 11(d), and 11(f)] show that this ovary could be easily classified as cancer as image data lies clearly on the cancer side of the linear decision boundary. Shape correction and application of reflectance data both reduced classification uncertainty by moving the data distribution further left of the boundary. Maps of the classification results in Fig. 11(c) and 11(e) confirm complete success in identifying the ovary as cancer. It is seen also that, for this particular ovary image, correction with reflectance data was unnecessary.

An example of an image of a normal ovary that was difficult to classify with LDA is given in Fig. 12. This ovary had a significant amount of adipose tissue on its surface. The classification based only on shape-corrected autofluorescence [Fig. 12(b)] gives mixed results. One can see that regions with more blood tend to misclassify. Figure 12(c) shows that dividing by the green reflectance image generally improves the classification in areas with more blood but leads to misclassification in adipose areas. This shows a limitation of our simple method of incorporating green reflectance data. Dealing with adipose tissue seems to require an algorithm that considers red and/or blue reflectance as well. Presence of adipose tissue on the ovaries appears uncommon, however, as it was only encountered for one set of ovaries in this study.

3.6 *Performance of Classification Mapping*

As a measure of the effectiveness of the MSI and classification scheme in performing *ex vivo* ovary diagnosis, we designed criteria to allow calculation of sensitivity and specificity of our diagnostic algorithm on the multispectral data. If 90% or more of the ROI pixels in an ovary image classified normal, we called the result a normal classification of the ovary. Vice versa, if 90% or more of the ROI pixels in an ovary image classified as cancer, we called this a cancer classification of the ovary. For any other percentage classification of the pixels in an ROI, the classification was called "indeterminate."

One hundred four images of 26 ovaries were classified for the first part of this study. From histopathology, 92 of these images (of 24 ovaries) were known from gross pathology to be normal, while 12 images (of two ovaries) were known to be cancer. The results of classification via LDA are presented in Table 2. Indeterminate classifications were treated the same as cancer classifications when calculating specificity and sensitivity. In all cases, intensity equalization was performed by scaling training set intensities using the ratio of mean 455-nm fluorescence of all normal training set measurements to normal test set measurements. The alternate method of intensity equalization based on the ratio of peak locations of fitted gamma distributions produced 30% lower specificity results and was abandoned. Jackknife analysis on the training data, Table 2, column one, represents an expectation of the highest sensitivity and specificity that can be achieved, as jackknife analysis on training data typically outperforms classification of a test set.

As shown in Table 2, sensitivity of 100% was achieved in all cases. We note, however, that two of 12 cancer images classified as indeterminant when data was not reflectance normalized, and this number improved to just one of 12 images when fluorescence measurements were divided by green reflectance.

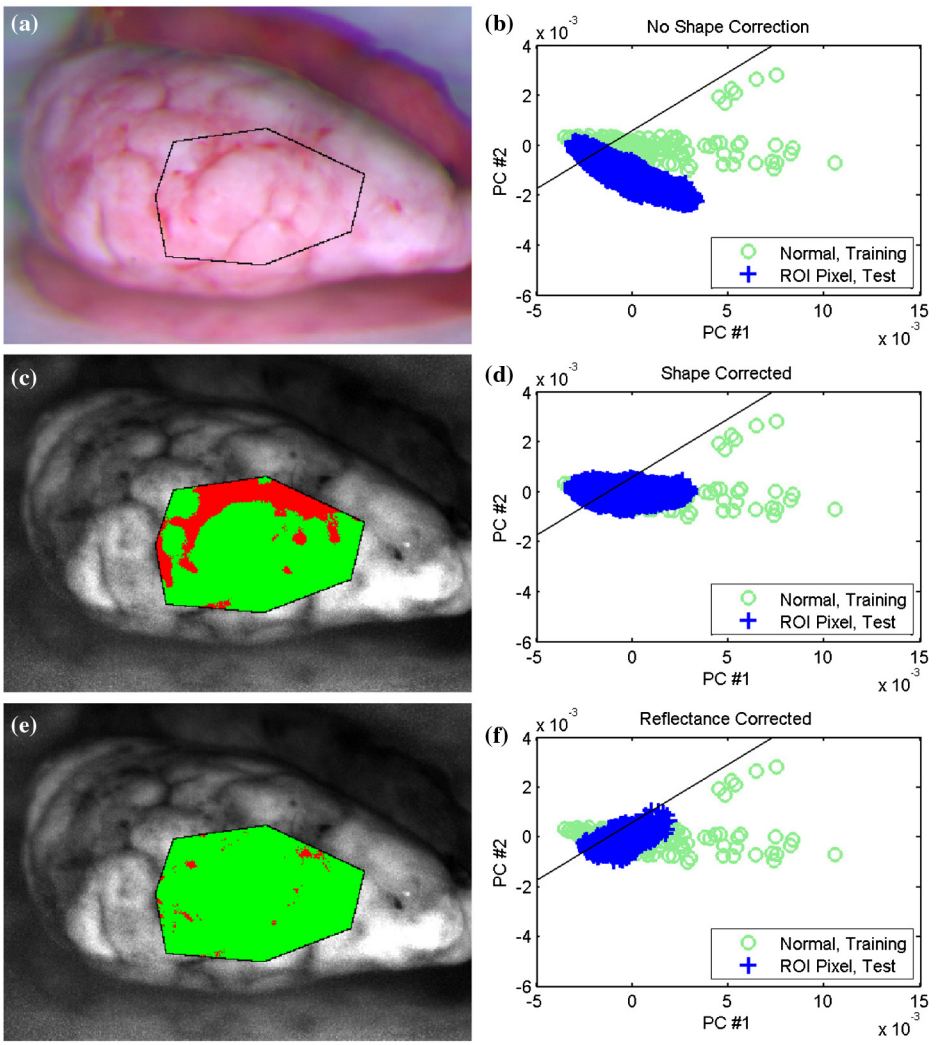

Fig. 10 (a) Crossed-polarization reflectance image of a normal ovary with ROI outlined. (b), (d), and (f) Multispectral autofluorescence image data plotted in two-PC space. Measurements at each ROI pixel of the ovary shown in (a) are plotted over normal measurements of the training set. Diagonal line represents a decision boundary for classification, with the upper left region corresponding to a cancer classification and lower right to a normal classification. (c) and (e) Tissue classification maps superimposed on fluorescence images of the same ovary. Green ROI pixels indicate normal classification. Red pixels indicate cancer classification. (b) Before spectral shape correction, pixel measurements do not overlap well with the training set. (c) and (d) After spectral shape correction, the data overlap well, but only 76% of pixels classify as normal. (e) and (f) After division by green channel reflectance, more than 97% of pixels classify as normal.

Although the number of cancerous ovaries in the study was small, the high sensitivity of the method is supported by the 100% sensitivity realized in the jackknife analysis of the training data, which included a larger number of cancerous measurements. Specificity when using the shape-corrected fluorescence data was considerably lower than predicted by jackknife analysis (51.1% versus 71.5%); however, dividing the fluorescence data by green reflectance improved the specificity to 68.5%, which is comparable to the jackknife analysis. To judge the benefit of imaging at multiple emission wavelength bands, we also performed classifications using single fluorescence bands. One such band chosen to classify with was the single filter wavelength 455 nm, which represented the peak of the measured eight-point fluorescence spectrum. We also tested classification with a wide fluorescence emission band formed by summing all eight points of the measured spectrum. Both of these simple cases produced reduced specificity, justifying the use of PCA and multispectral measurements.

3.7 *Excluded Measurements and Benign Classification Results*

Images of 14 of 49 resected ovaries were necessarily excluded from classification. Five were excluded because of extensive external blood on the ovarian surface. Three were excluded because of dye present from another study. Three were excluded because of device malfunction or improper setting. Two were excluded because, although cancerous, the ovaries had been invaded by a cancer that originated elsewhere in the body. Finally, one ovary image set was excluded because tumor growth was so extensive that no ovary remnant could be identified.

Table 2 classification results include only the normal and cancer ovaries, or 26 of the 35 ovaries analyzed. Nine ovaries of a benign neoplasm or endometriosis pathology designation were also imaged. An identical classification of these nine ovaries into normal or cancer classes was performed using the same training data. All 10 benign neoplasm ovary images classified as

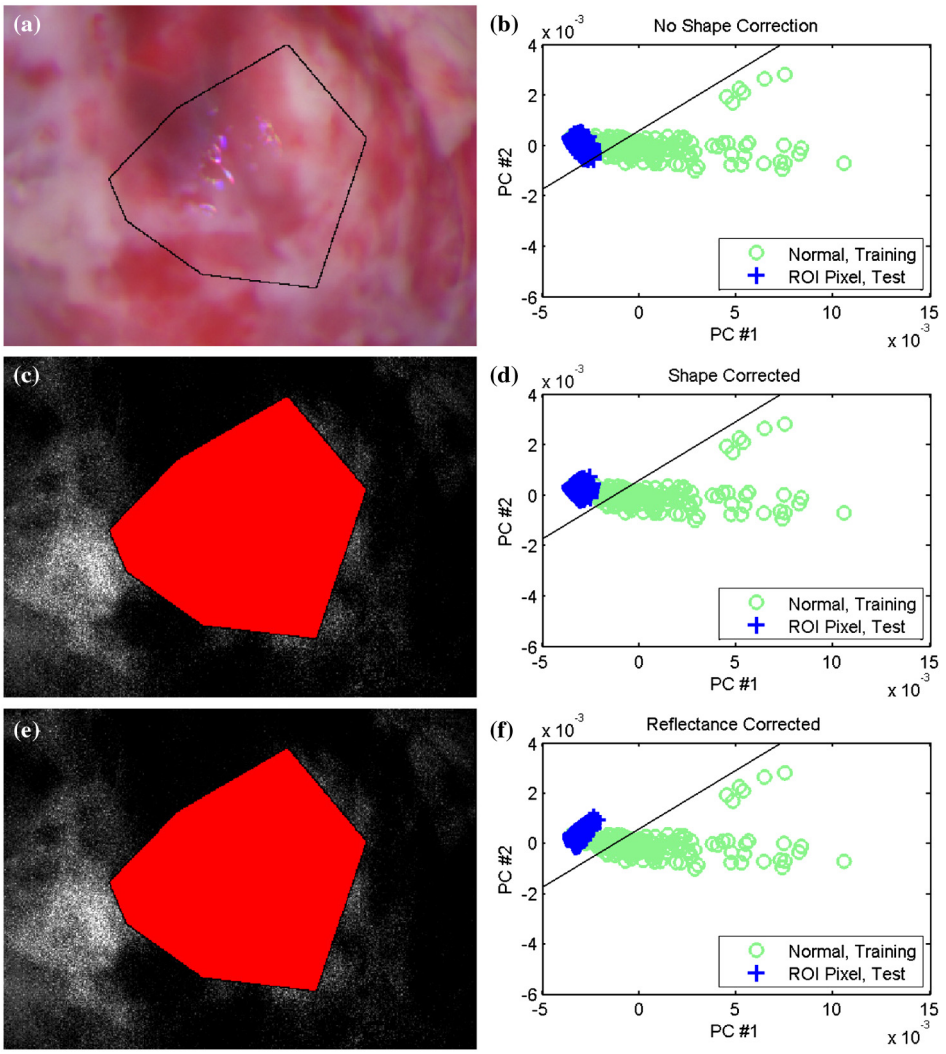

Fig. 11 (a) Crossed-polarization reflectance image of a large cancer ovary with ROI outlined. (b), (d), and (f) Multispectral autofluorescence image data plotted in two-PC space. Measurements at each ROI pixel of the ovary shown in (a) are plotted over normal measurements of the training set. Diagonal line represents a decision boundary for classification, with the upper left region corresponding to a cancer classification and lower right to a normal classification. (c) and (e) Tissue classification maps superimposed on fluorescence images of the same ovary. Green ROI pixels indicate normal classification. Red pixels indicate cancer classification. (b) Before spectral shape correction, pixel measurements of this ovary already fall on the cancer side of the decision boundary. (c) and (d) After spectral shape correction, 100% of pixels classify as cancer. (e) and (f) After division by green channel reflectance, pixel measurements lie farther to the cancer side of the decision boundary.

normal, whereas the 30 images of endometriosis ovaries were evenly split with 10 normal classifications, nine cancer, and 11 indeterminate.

4 Discussion and Conclusions

We have demonstrated that previously collected single-point autofluorescence measurements of tissue biopsies can be used in combination with newly acquired multispectral images of fresh surgical specimens to effectively diagnose macroscopic areas of tissue. Although single-point fluorescence data were collected in the form of a high-resolution EEM, we transformed them for comparison with eight-point fluorescence spectra captured by the MSI. We created pixel-by-pixel diagnostic maps of the imaged tissue, incorporating the independent, single-point measurements of similar tissues as training data for LDA classification of MSI-measured spectra.

Spectral shape correction was required for effective classification because, although both devices were calibrated for their individual spectral responses and their measurement intensities equalized, the average MSI-collected and probe-collected spectra were different [Fig. 6(a) and 6(b)]. Specifically, the MSI appeared to collect lower relative fluorescence in the violet emission region (especially 420 nm) and to emphasize the longest emission wavelengths (>500 nm). The peak of the average eight-point spectrum was redshifted by one point (from 455 to 485 nm). Redshift of imager-collected spectra relative to probe-collected spectra has been reported by others[43,46] and is believed to occur due to differences in the illumination-collection geometries of spectral imager and spectroscopic probe. Gebhart et al.[43] determined that the illumination-collection geometry of their imager, on average, led to collected photons with increased tissue interaction compared to those collected by their probe system. We show here that simple shape correction of imaging

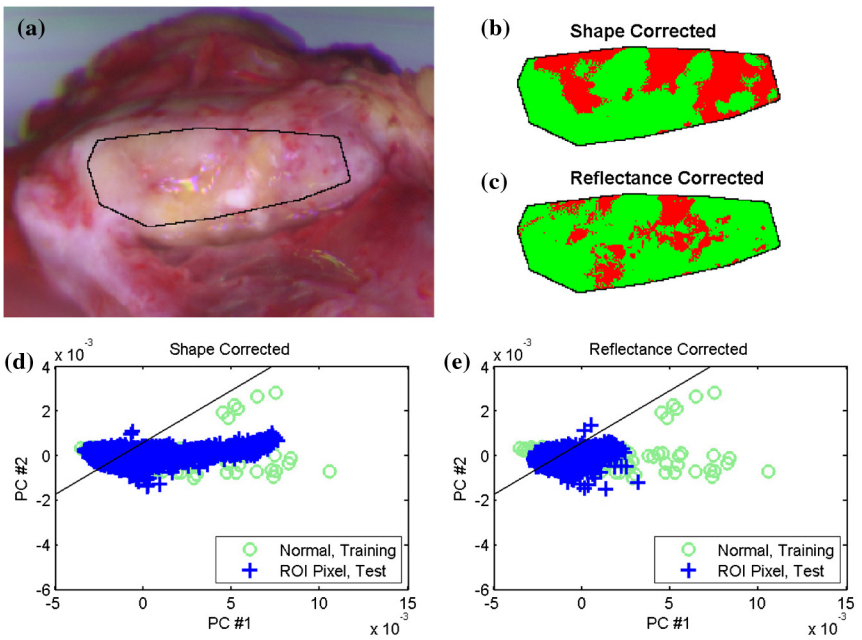

Fig. 12 (a) Crossed-polarization reflectance image of a normal ovary with ROI outlined. Adipose tissue is prevalent on the ovary. (b) and (c) Tissue classification maps over the ROI of same ovary. Green ROI pixels indicate normal classification. Red pixels indicate cancer classification. Classification using shape-corrected fluorescence data is poor. Classification improves with incorporation of green reflectance data, but areas high in adipose tissue tend to misclassify. (d) and (e) Multispectral autofluorescence image data plotted in two-PC space. Pixel measurements fall on both sides of the decision boundary.

spectra for one-to-one comparison with single-point spectra produces good agreement for classification.

Ovary autofluorescence images were divided by normalized, crossed-polarization, green reflectance band images to compensate for spatial variations in the tissue optical properties caused by hypervascular areas and surface blood. The division-by-reflectance method is similar to reported corrections of tissue fluorescence spectra[44,47] and images.[45,48] During initial classifications, without this correction, very low fluorescence was measured from reddened tissue areas and resulted in misclassification of those portions of normal ovaries as cancer. Since we required 90% of image ROI pixels to classify correctly for a successful overall classification of the ovary, a number of false positives resulted without the correction, and specificity was 51.1%. Applying the division-by-reflectance correction improved the specificity to 68.5% without changing the sensitivity (100%) and placed classification performance on the level predicted by training set jackknife analysis (100%/71.5%).

It should be noted that no reflectance measurements existed for the single-point autofluorescence training set, and thus it was not possible to correct the training data in the same manner as the MSI data. We justify classification of the reflectance-modified test set using the unmodified training set by noting that reflectance images were individually normalized (given mean pixel value of one) before the division, maintaining the fluorescence images' average intensities. Surface blood and hypervascular tissue areas also likely had less influence on the training set data, which were collected by a probe interrogating small (< 1 mm diameter), carefully selected tissue areas. As a result of the normalization of the reflectance images used for correction, tissue optical property spatial variations within particular images were compensated, but image-to-image and ovary-to-ovary tissue optical property variations were not.

Classification of ovarian tissue images based on 365-nm excitation autofluorescence alone does not appear to be sufficient as a technique for diagnosis of ovarian cancer because although sensitivity of the technique was high, specificity was low (51.1%). Blood in the ROI appeared to be the major confounder in about half of the normal ovary images that misclassified. The cause of the other half of misclassifications is unclear but may be due to general variation of tissue optical properties. Correction by green reflectance data led to a more useful specificity of 68.5%. Still higher specificity is desired

Table 2 Classification results using linear discriminant analysis.

	Single-point training spectra	Fluorescence	Fluorescence/green reflectance	Summed fluorescence	455 nm fluor. only
Sensitivity %	100[a]	100[b]	100[b]	100[b]	100[b]
Specificity %	71.5	51.1	68.5	38.0	31.5

[a]Based on 211 single-point measurements; 25 measurements of 10 cancerous ovaries and 186 measurements of 65 normal ovaries (typically three per biopsy).
[b]Based 104 images of 26 ovaries; 12 images of two cancerous ovaries and 92 images of 24 normal ovaries (typically three to five images per ovary).

and might be obtainable in an imager using more than one excitation wavelength. Spectroscopic studies of the cervix[49] and ovary[50] have demonstrated higher specificities than obtained here, but these incorporated multiple excitation wavelengths to target various endogenous fluorophores. A second alternative to combat the problems associated with blood and tissue optical property variation would be to use FLIM, which is less sensitive to these confounders. Such a system, however, would be more complex, more expensive, and require longer acquisition times.

In this study we have found that benign neoplasm ovaries could be correctly classified as nonmalignant with a normal versus cancer binary classification. This result makes the diagnostic findings on normal and cancer ovaries more meaningful. Endometriosis ovaries, however, are frequently misclassified as malignant in such a binary test. Presumably this result stems from discoloration of the ovary and additional absorption of fluorescence with the presence of additional near-surface vasculature. Our approach of correcting for tissue absorption differences with division by green reflectance data was insufficient to classify endometriosis ovary images as nonmalignant in the binary classification.

All of the measurements used in this study, both single-point and from imaging, have been performed *ex vivo*. *In vivo* ovary measurements[4,51] as well as *ex vivo* imaging[41,52] have been reported previously by our research group. A long-term goal of the authors is to integrate this technology into laparoscopy for *in vivo* diagnostics and real-time cancer screening of individuals at high risk for developing ovarian cancer. Real-time versions of the diagnostic device will not use manual selection of an ROI, but rather classify tissue over a predefined portion of the field of view. Classification maps would be acquired at discretion of the surgeon because of the need to expose tissue to ultraviolet light. If high sensitivity of this technique is confirmed with *in vivo* studies, the optimal time point of prophylactic oophorectomy could be determined. The described method also would appear to be useful in tumor delineation or selective oophorectomy (only one ovary removed). Additional studies including coordinated sectioning and histopathology would further determine the value of adding multispectral capabilities to endoscopy.

Acknowledgments

We would like to acknowledge the assistance and inputs of Dr. Steve Saggese, Dr. Greg Mooradian, and others at QinetiQ North America. The SEAtreat MSI system used to collect data for this paper was provided by QinetiQ North America and development funded by the United States Army Medical Research and Materiel Command, Telemedicine and Advanced Technical Research Center (TATRC), under Grants DAMD17-02-1-0635 and W81XWH-08-1-0086. We also wish to thank our research nurse Kathy Schmidt for her contributions to the clinical study. Funding for the research described in this paper was provided under grants NIH/NCI R01CA098341, T32EB000809, the Arizona Cancer Center, Better than Ever Ovarian Cancer Research Program, and TRIF imaging fellowship.

References

1. Cancer Facts & Figures 2010, American Cancer Society, Atlanta (2010).
2. N. Auersperg et al., "Ovarian surface epithelium: biology, endocrinology, and pathology," *Endocr. Rev.* **22**(2), 255–288 (2001).
3. R. Richards-Kortum and E. Sevick-Muraca, "Quantitative optical spectroscopy for tissue diagnosis," *Annu. Rev. Phys. Chem.* **47**, 555–606 (1996).
4. M. Brewer et al., "Fluorescence spectroscopy for in vivo characterization of ovarian tissue," *Lasers Surg. Med.* **29**(2), 128–135 (2001).
5. T. G. Papazoglou, "Malignancies and atherosclerotic plaque diagnosis—is laser induced fluorescence spectroscopy the ultimate solution?" *J. Photochem. Photobiol. B* **28**(1), 3–11 (1995).
6. I. J. Bigio and J. R. Mourant, "Ultraviolet and visible spectroscopies for tissue diagnostics: fluorescence spectroscopy and elastic-scattering spectroscopy," *Phys. Med. Biol.* **42**(5), 803–814 (1997).
7. G. A. Wagnieres, W. M. Star, and B. C. Wilson, "In vivo fluorescence spectroscopy and imaging for oncological applications," *Photochem. Photobio.* **68**(5), 603–632 (1998).
8. N. Ramanujam, "Fluorescence spectroscopy of neoplastic and non-neoplastic tissues," *Neoplasia* **2**(1–2), 89–117 (2000).
9. R. Marchesini et al., "*In vivo* spectrophotometric evaluation of neoplastic and non-neoplastic skin pigmented lesions, I. reflectance measurements," *Photochem. Photobiol.* **53**(1), 77–84 (1991).
10. V. P. Wallace et al., "Spectrophotometric assessment of pigmented skin lesions: methods and feature selection for evaluation of diagnostic performance," *Phys. Med. Biol.* **45**(3), 735–751 (2000).
11. C. Zhu et al., "Diagnosis of breast cancer using diffuse reflectance spectroscopy: comparison of a Monte Carlo versus partial least squares analysis based feature extraction technique," *Lasers. Surg. Med.* **38**(7), 714–724 (2006).
12. C. Zhu et al., "Diagnosis of breast cancer using fluorescence and diffuse reflectance spectroscopy: a Monte-Carlo-model-based approach," *J. Biomed. Opt.* **13**(3), 034015 (2008).
13. G. M. Palmer et al., "Comparison of multiexcitation fluorescence and diffuse reflectance spectroscopy for the diagnosis of breast cancer," *IEEE Trans. Biomed. Eng.* **50**(11), 1233–1242 (2003).
14. T. M. Breslin et al., "Autofluorescence and diffuse reflectance properties of malignant and benign breast tissues," *Ann. Surg. Oncol.* **11**(1), 65–70 (2004).
15. C. Zhu et al., "Use of a multiseparation fiber optic probe for the optical diagnosis of breast cancer," *J. Biomed. Opt.* **10**(2), 024032 (2005).
16. S. K. Majumder et al., "A probability-based spectroscopic diagnostic algorithm for simultaneous discrimination of brain tumor and tumor margins from normal brain tissue," *Appl. Spectrosc.* **61**(5), 548–557 (2007).
17. W. C. Lin et al., "*In vivo* brain tumor demarcation using optical spectroscopy," *Photochem. Photobiol.* **73**(4), 396–402 (2001).
18. S. C. Gebhart, W. C. Lin, and A. Mahadevan-Jansen, "*In vitro* determination of normal and neoplastic human brain tissue optical properties using inverse adding-doubling," *Phys. Med. Biol.* **51**(8), 2011–2027 (2006).
19. C. R. Weber et al., "Model-based analysis of reflectance and fluorescence spectra for in vivo detection of cervical dysplasia and cancer," *J. Biomed. Opt.* **13**(6), 064016 (2008).
20. V. T. Chang et al., "Quantitative physiology of the precancerous cervix *in vivo* through optical spectroscopy," *Neoplasia* **11**(4), 325–332 (2009).
21. Y. N. Mirabal et al., "Reflectance spectroscopy for in vivo detection of cervical precancer," *J. Biomed. Opt.* **7**(4), 587–594 (2002).
22. B. Palcic et al., "Detection and localization of early lung cancer by imaging techniques," *Chest* **99**(3), 742–743 (1991).
23. R. D. Alvarez and T. C. Wright Jr., "Increased detection of high-grade cervical intraepithelial neoplasia utilizing an optical detection system as an adjunct to colposcopy," *Gynecol. Oncol.* **106**(1), 23–28 (2007).
24. K. Gono, "Multifunctional endoscopic imaging system for support of early cancer diagnosis," *IEEE J. Sel. Top. Quant. Electron.* **14**(1), 62–69 (2008).
25. C. Balas, "Review of biomedical optical imaging-a powerful, non-invasive, non-ionizing technology for improving in vivo diagnosis," *Meas. Sci. Tech.* **20**(10), 104020 (2009).
26. P. M. Lane et al., "Simple device for the direct visualization of oral-cavity tissue fluorescence," *J. Biomed. Opt.* **11**(2), 024006 (2006).
27. J. Mizeret et al., "Instrumentation for real-time fluorescence lifetime imaging in endoscopy," *Rev. Sci. Instrum.* **70**(12), 4689–4701 (1999).
28. K. König, "Clinical multiphoton tomography," *J. Biophot.* **1**(1), 13–23 (2008).

29. Y. Sun et al., "Fluorescence lifetime imaging microscopy: in vivo application to diagnosis of oral carcinoma," *Opt. Lett.* **34**(13), 2081–2083 (2009).
30. Y. Sun et al., "Fluorescence lifetime imaging microscopy for brain tumor image-guided surgery," *J. Biomed. Opt.* **15**(5), 056022–056025 (2010).
31. P. Yang et al., "Macroscopic spectral imaging and gene expression analysis of the early stages of melanoma," *Mol. Med.* **5**(12), 785–794 (1999).
32. C. Balas, "A novel optical imaging method for the early detection, quantitative grading, and mapping of cancerous and precancerous lesions of cervix," *IEEE Trans. Biomed. Eng.* **48**(1), 96–104 (2001).
33. S. G. Kong et al., "Hyperspectral fluorescence image analysis for use in medical diagnostics," *Proc. SPIE* **5692**, 21–28 (2005).
34. S. Y. Park et al., "Automated image analysis of digital colposcopy for the detection of cervical neoplasia," *J. Biomed. Opt.* **13**(1), 014029 (2008).
35. C. C. Yu et al., "Quantitative spectroscopic imaging for non-invasive early cancer detection," *Opt. Express* **16**(20), 16227–16239 (2008).
36. D. Roblyer et al., "Objective detection and delineation of oral neoplasia using autofluorescence imaging," *Canc. Prev. Res.* **2**(5), 423–431 (2009).
37. W. P. Soutter et al., "Dynamic spectral imaging: improving colposcopy," *Clin. Canc. Res.* **15**(5), 1814–1820 (2009).
38. M. D. Tocci, "Multiple Imaging System," US Patent 6,856,466 , USPTO, Ed. (2005).
39. M. D. Tocci, N. C. Tocci, and G. C. Mooradian, "Multiple Imaging System and Method for Designing Same," US Patent 7,177,085 , USPTO, Ed. (2007).
40. G. M. Palmer et al., "Optimal methods for fluorescence and diffuse reflectance measurements of tissue biopsy samples," *Lasers Surg. Med.* **30**(3), 191–200 (2002).
41. M. A. Brewer et al., "Imaging of the ovary," *Tech. Canc. Res. Treat.* **3**(6), 617–627 (2004).
42. M. Michaelides, "Early detection of ovarian cancer using fluorescence spectroscopy and parallel factor analysis," Master's Thesis, University of Arizona (2007).
43. S. C. Gebhart, S. K. Majumder, and A. Mahadevan-Jansen, "Comparison of spectral variation from spectroscopy to spectral imaging," *Appl. Opt.* **46**(8), 1343–1360 (2007).
44. H. Zeng et al., "Spectroscopic and microscopic characteristics of human skin autofluorescence emission," *Photochem. Photobiol.* **61**(6), 639–645 (1995).
45. J. Y. Qu, Z. Huang, and J. Hua, "Excitation-and-collection geometry insensitive fluorescence imaging of tissue-simulating turbid media," *Appl. Opt.* **39**(19), 3344–3356 (2000).
46. M. D. Keller et al., "Autofluorescence and diffuse reflectance spectroscopy and spectral imaging for breast surgical margin analysis," *Lasers Surg. Med.* **42**(1), 15–23 (2010).
47. W.-C. Lin et al., "Intraoperative application of optical spectroscopy in the presence of blood," *IEEE J. Sel. Top. Quant. Electron.* **7**(6), 996–1003 (2001).
48. T. Wu et al., "Preliminary study of detecting neoplastic growths in vivo with real time calibrated autofluorescence imaging," *Opt. Express* **11**(4), 291–298 (2003).
49. N. Ramanujam et al., "Cervical precancer detection using a multivariate statistical algorithm based on laser-induced fluorescence spectra at multiple excitation wavelengths," *Photochem. Photobiol.* **64**(4), 720–735 (1996).
50. R. George et al., "Parallel factor analysis of ovarian autofluorescence as a cancer diagnostic," *Lasers Surg. Med.* (2012).10.1002/lsm.22014.
51. U. Utzinger et al., "Reflectance spectroscopy for in vivo characterization of ovarian tissue," *Lasers Surg. Med.* **28**(1), 56–66 (2001).
52. N. D. Kirkpatrick, M. A. Brewer, and U. Utzinger, "Endogenous optical biomarkers of ovarian cancer evaluated with multiphoton microscopy," *Canc. Epid. Biomark. Prev.* **16**(10), 2048–2057 (2007).